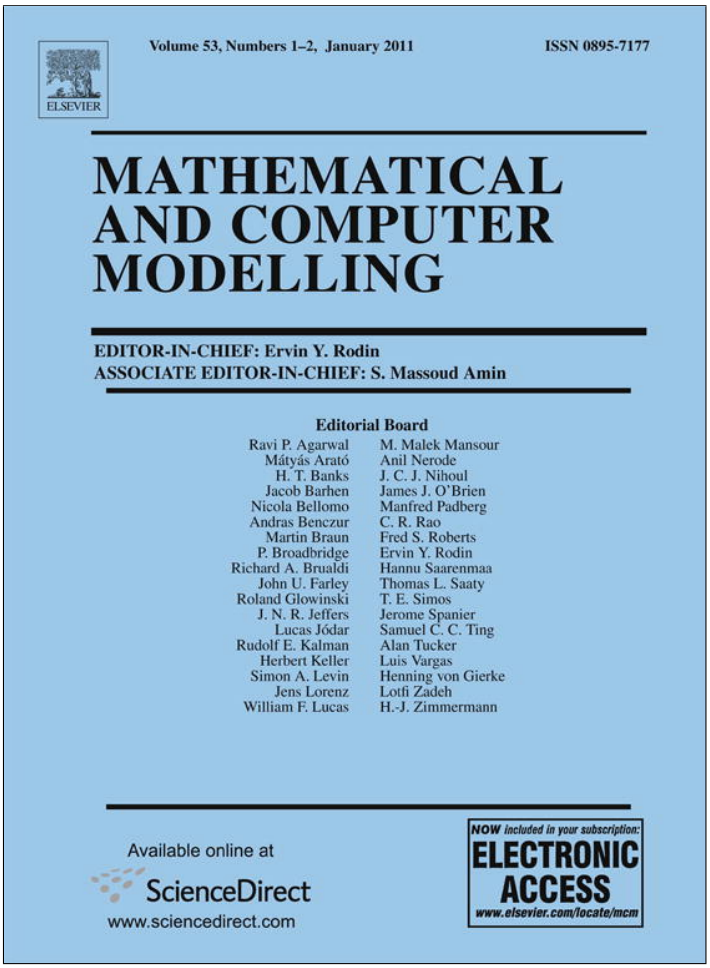

Mathematical and Computer Modelling 53 (2011) 269–279

Contents lists available at ScienceDirect

Mathematical and Computer Modelling

journal homepage: www.elsevier.com/locate/mcm

# Artificial viscosity proper orthogonal decomposition

Jeff Borggaard, Traian Iliescu *, Zhu Wang

*Department of Mathematics, Virginia Polytechnic Institute and State University, Blacksburg, VA 24061, USA*

ARTICLE INFO

*Article history:*
Received 13 July 2010
Accepted 13 August 2010

*Keywords:*
Proper orthogonal decomposition
Large eddy simulation
Artificial viscosity

ABSTRACT

We introduce improved reduced-order models for turbulent flows. These models are inspired from successful methodologies used in large eddy simulation, such as artificial viscosity, applied to standard models created by proper orthogonal decomposition of flows coupled with Galerkin projection. As a first step in the analysis and testing of our new methodology, we use the Burgers equation with a small diffusion parameter. We present a thorough numerical analysis for the time discretization of the new models. We then test these models in two problems displaying shock-like phenomena. Of course, since the Burgers equation does not model turbulence, we next need to test our new models in realistic turbulent flow settings. This is the subject of a forthcoming report.



## 1. Introduction

Dynamical system ideas have recently gained increased momentum in the field of fluid dynamics [1,2]. In turbulent flows, these ideas are of particular interest. Indeed, dynamical systems could be used to describe low-dimensional structures that play an important role in the dynamics of the flow, such as the coherent structures in the turbulent boundary layer, which are believed to be central in understanding the mechanism of turbulence.

One of the most successful dynamical system ideas in the study of turbulent flows has been the *Proper Orthogonal Decomposition (POD)* [3–6]. POD starts with data from an accurate numerical simulation and extracts the most energetic modes in the system by using the singular value decomposition. POD has been used to generate reduced-order models for the prediction and control of turbulent flows [7–15]. Aubry et al. proposed in [7] a low-dimensional model to approximate the coherent structures in the turbulent boundary layer. This model has truncated the POD basis and has used a mixing-length type approximation to model the effect of the discarded POD modes on the POD modes kept in the model. The model has yielded good qualitative results, considering the coarseness of the approximation. In [16,17], it was shown that the model reproduced qualitatively well the physics of the turbulent boundary layer and that by adding new POD modes, the accuracy of the model was increased.

The model in [7] relies fundamentally on the assumption of *energy cascade*, which states that energy flows from large scales to small scales. This concept has been thoroughly tested experimentally and numerically and has played a central role in the large eddy simulation of turbulent flows. The validity of the extension of the concept of energy cascade from the Fourier space setting to the POD setting has been investigated in [18]. In this numerical study, it was shown that there is a net forward energy transfer from low index POD modes to higher index POD modes.

The studies in [7,16–18] represent the motivation of our present study. They clearly suggest that the concept of energy cascade is also valid in a POD setting. Therefore, LES ideas based on the concept of energy cascade could also be used in devising reduced-order models in a POD context. Our current study proposes the use of the *artificial viscosity* as a means

* Corresponding author.
*E-mail addresses:* jborggaard@vt.edu (J. Borggaard), iliescu@vt.edu (T. Iliescu), wangzhu@vt.edu (Z. Wang).
*URLs:* http://www.math.vt.edu/people/borggajt (J. Borggaard), http://www.math.vt.edu/people/iliescu (T. Iliescu), http://www.math.vt.edu/people/wangzhu (Z. Wang).

0895-7177/$ – see front matter © 2010 Elsevier Ltd. All rights reserved.
doi:10.1016/j.mcm.2010.08.015

of improving the reduced-order POD model in [7]. As a first step in a thorough theoretical and numerical investigation of these new artificial viscosity POD models, we use the Burgers equation with a small viscosity parameter. We emphasize that the Burgers equation does not represent turbulence. We use it, however, for simplicity and clarity of exposition. Of course, to assess the success of our new methodology, we will next investigate it in the numerical simulation of realistic turbulent flows.

The rest of the paper is organized as follows. In Section 2, we briefly describe the POD methodology. Section 3 introduces the new POD artificial viscosity model. The error analysis for the time discretization of the new model is presented in Section 4. The new methodology is tested numerically in Section 5 for two problems displaying shock-like phenomena. Finally, Section 6 presents the conclusions and future research directions.

## 2. Proper orthogonal decomposition

In this section, we briefly describe the *proper orthogonal decomposition (POD)*, following [19]. For a detailed presentation, the reader is referred to [3–6].

Let $\mathcal{H}$ be a real Hilbert space endowed with the inner product $(\cdot,\cdot)_{\mathcal{H}}$, and $u(\cdot,t)\in\mathcal{H}$, $t\in[0,T]$ be the state variable of a dynamical system. Given the time instances $t_1,\ldots,t_n\in[0,T]$, we consider the ensemble of snapshots

$$\mathcal{V} := \operatorname{span}\{u(\cdot,t_1),\ldots,u(\cdot,t_n)\},$$

with $\dim\mathcal{V}=d$. The POD seeks a low-dimensional $(r)$ basis $\{\varphi_1,\ldots,\varphi_r\}$ that optimally approximates the input collection in the sense

$$\min \frac{1}{n}\sum_{i=1}^{n}\left\|u(\cdot,t_i)-\sum_{j=1}^{r}(u(\cdot,t_i),\varphi_j(\cdot))_{\mathcal{H}}\,\varphi_j(\cdot)\right\|_{\mathcal{H}}^2 \tag{1}$$

subject to the conditions that $(\varphi_i,\varphi_j)_{\mathcal{H}}=\delta_{ij}$, $1\le i,j\le r$. In order to solve (1), we consider the eigenvalue problem

$$Kv=\lambda v, \tag{2}$$

where $K\in\mathbb{R}^{n\times n}$, with $K_{ij}=\frac{1}{n}(u(\cdot,t_j),u(\cdot,t_i))_{\mathcal{H}}$, is the snapshot correlation matrix, $v_k$, $k=1,\ldots,n$ are the eigenvectors, and $\lambda_1\ge\lambda_2\ge\cdots\ge\lambda_d>0$ are the positive eigenvalues. It can then be shown (see [3–6]), that the solution of (1) is given by

$$\varphi_k(\cdot)=\frac{1}{\sqrt{\lambda_k}}\sum_{j=1}^{n}(v_k)_j\,u(\cdot,t_j),\quad 1\le k\le r, \tag{3}$$

where $(v_k)_j$ is the $j$-th component of the eigenvector $v_k$. It can also be shown that the following error formula holds

$$\frac{1}{n}\sum_{i=1}^{n}\left\|u(\cdot,t_i)-\sum_{j=1}^{r}(u(\cdot,t_i),\varphi_j(\cdot))_{\mathcal{H}}\,\varphi_j(\cdot)\right\|_{\mathcal{H}}^2=\sum_{j=r+1}^{d}\lambda_j. \tag{4}$$

In what follows, we will use the notation $S^r=\operatorname{span}\{\varphi_1,\varphi_2,\ldots,\varphi_r\}$.

## 3. Artificial viscosity POD model

In this section, we present the artificial viscosity POD model. To this end, we start by introducing some notation.

The mathematical model we consider is the *Burgers equation*

$$\begin{cases} u_t-\nu\,u_{xx}+u\,u_x=f & \text{in } \Omega,\\ u(x,0)=u_0(x) & \text{in } \Omega,\\ u(x,t)=g(x,t) & \text{on } \partial\Omega, \end{cases} \tag{5}$$

where $\nu$ is the diffusion parameter, $f$ the forcing term, $\Omega\subset\mathbb{R}$ the computational domain, $t\in[0,T]$, with $T$ the final time, $u_0(\cdot)$ the initial condition, and $g(\cdot)$ the boundary conditions. Without loss of generality, we assume that $g=0$ in what follows. We emphasize that Burgers equation (5), while being commonly used as a one-dimensional approximation of the Navier–Stokes equations, does not model turbulence. We use it, however, for simplicity and clarity of exposition.

Let $L^2$, $H_0^1$, $W^{1,3}$, $W_0^{1,3}$ denote the usual Sobolev spaces on $\Omega$ [20] and $(\cdot,\cdot)=(\cdot,\cdot)_{L^2}$. Let $a:H_0^1\times H_0^1\to\mathbb{R}$ be defined as

$$a(\varphi,\psi):=\nu(\varphi',\psi')\quad\forall\varphi,\psi\in H_0^1. \tag{6}$$

For all $\varphi,\psi\in H_0^1$, we define

$$(F(\varphi),\psi):=(\varphi\varphi',\psi). \tag{7}$$

Furthermore, for $\varphi, \psi \in W^{1,3}$ and $c$ a positive constant, we define

$$(G(\varphi), \psi) := c\,(|\varphi'|\varphi', \psi'). \tag{8}$$

Let $u_0 \in L^2$ and $f \in \mathcal{C}(0, T; L^2)$. Then the weak formulation of (5) reads

$$\begin{cases} (u_t, \varphi) + a(u, \varphi) + (F(u), \varphi) = (f, \varphi) & \forall \varphi \in H_0^1, \\ (u(0), \chi) = (u_0, \chi) & \forall\, \chi \in L^2. \end{cases} \tag{9}$$

We denote the time-step $\Delta t := T/m$ and the time instances $t_k = k\Delta t,\ k = 0, 1, \ldots, m$. Following [19], we consider the following $2m + 1$ snapshots

$$\{u(t_0),\ u(t_1), \ldots, u(t_m), \overline{\partial} u(t_1), \ldots, \overline{\partial} u(t_m)\}, \tag{10}$$

where $\overline{\partial} u(t_k) = \frac{u(t_k) - u(t_{k-1})}{\Delta t}$. As explained in [19], we included $\overline{\partial} u(t_k)$ in the set of snapshots in order to avoid an extra $(\Delta t)^{-2}$ factor in the error estimates.

By using the backward Euler method for the time discretization and denoting $\overline{\partial} U_k = \frac{U_k - U_{k-1}}{\Delta t}$, the POD Galerkin truncation of (9) is

$$\begin{cases} (\overline{\partial} U_k, \varphi) + a(U_k, \varphi) + (F(U_k), \varphi) = (f(t_k), \varphi) & \forall \varphi \in S^r, \\ (U_0, \chi) = (u_0, \chi) & \forall\, \chi \in S^r. \end{cases} \tag{11}$$

As mentioned in the introduction, in turbulent flow computations, such a simple POD Galerkin truncation would not suffice. The model we propose herein is an improvement of the mixing-length model in [7]. Specifically, we use an artificial viscosity term similar to the one used in the Smagorinsky model [21], which yields the artificial viscosity Burgers equation

$$\begin{cases} (u_t, \varphi) + a(u, \varphi) + (F(u), \varphi) + (G(u), \varphi) = (f, \varphi) & \forall \varphi \in W_0^{1,3}, \\ (u(0), \chi) = (u_0, \chi) & \forall\, \chi \in L^2. \end{cases} \tag{12}$$

This approach yields the following *artificial viscosity (AV) POD* model, which we will denote POD–AV

$$\begin{cases} (\overline{\partial} U_k, \varphi) + a(U_k, \varphi) + (F(U_k), \varphi) + (G(U_k), \varphi) = (f(t_k), \varphi) & \forall \varphi \in S^r, \\ (U_0, \chi) = (u_0, \chi) & \forall\, \chi \in S^r. \end{cases} \tag{13}$$

We emphasize again that, since we illustrate our new model in the context of the Burgers equation, its role is somehow different from its original purpose. Indeed, in the numerical simulation of turbulent flows, the POD–AV model (13) should dissipate energy according to the well known concept of energy cascade [22,23]. In the context of the Burgers equation, however, the POD–AV model's role is to stabilize the numerical solution in test problems displaying shock-like behavior.

## 4. Error estimates

In this section, we prove estimates for the error $\frac{1}{m}\sum_{k=1}^{m} \|U_k - u(t_k)\|^2$, where the approximation $U_k$ is the solution of (13) and $u(t_k)$ is the solution of (12). To this end, we follow the presentation in [19]. We emphasize that, although the general approach that we use is that in [19], there are several differences stemming from the nonlinear AV term that was not present in the formulation found in [19]. We also note that the error estimates in this paper, as well as those in [19,24], only concern the time discretization and the POD truncation. For a finite element spatial discretization error analysis and alternative error estimates, the reader is referred to [25,26], respectively.

We start by listing several results that will be used throughout this section. The first is the Poincaré inequality: there exists a constant $\alpha > 0$ such that the following relationship between the $L^2$-norm and the $H^1$-seminorm holds

$$\|\varphi\|^2 \le \alpha\, |\varphi|_1^2 \quad \forall \varphi \in H_0^1. \tag{14}$$

The bilinear form $a(\cdot, \cdot)$ is continuous and coercive: there exist constants $\beta$ and $\kappa$ such that

$$|a(\varphi, \psi)| \le \beta \|\varphi\|_1 \|\psi\|_1 \quad \forall \varphi,\ \psi \in H_0^1 \tag{15}$$

$$|a(\varphi, \varphi)| \ge \kappa\, \|\varphi\|_1^2 \quad \forall \varphi \in H_0^1. \tag{16}$$

We will also use the following lemma [27,28]:

**Lemma 4.1** (*Strong Monotonicity and Lipschitz Continuity of G*). *For all $\varphi_1, \varphi_2, \psi \in W^{1,3}$, there exists a generic constant $C$ independent of $\varphi_1, \varphi_2$ or $\psi$, such that the following inequalities hold:*

$$(G(\varphi_1) - G(\varphi_2), (\varphi_1 - \varphi_2)) \ge C\, \|(\varphi_1 - \varphi_2)'\|_{L^3}^3, \tag{17}$$

$$(G(\varphi_1) - G(\varphi_2), \psi) \le C\, M\, \|(\varphi_1 - \varphi_2)'\|_{L^3}\, \|\psi'\|_{L^3}, \tag{18}$$

*where* $M := \max\left\{\|\varphi_1'\|_{L^3}, \|\varphi_2'\|_{L^3}\right\}$.

Using the strong monotonicity of $G$ (17) and following [29–31], one can prove that both (12) and (13) have a unique solution.

For clarity of notation, we will denote by $C_k$, $k \in \mathbb{N}$, a generic constant that can depend on all the parameters in the system, except on $r$ (the number of POD modes retained in the Galerkin truncation) and $m$ (the number of snapshots).

We define the projection $P^r : H_0^1 \to S^r$ as follows: For all $u \in H_0^1$,

$$a(P^r u, \psi) = a(u, \psi) \quad \forall \psi \in S^r. \tag{19}$$

For $\Delta t$ small enough, the projection operator $P^r$ has the following approximation properties [19]:

$$\frac{1}{m} \sum_{k=1}^{m} \|u(t_k) - P^r u(t_k)\|_1^2 \le C_1 \sum_{k=r+1}^{d} \lambda_k, \tag{20}$$

$$\frac{1}{m} \sum_{k=1}^{m} \|\overline{\partial} u(t_k) - P^r \overline{\partial} u(t_k)\|_1^2 \le C_2 \sum_{k=r+1}^{d} \lambda_k. \tag{21}$$

We will also be using the following inverse estimate:

**Lemma 4.2.** *There exist constants $C_3$ and $C_4$, such that, for all $v \in \mathcal{V}$, the following inequalities hold*

$$\|v\|_{L^3} \le C_3 \|v\|_{L^2} \quad \text{and} \quad \|v\|_{L^2} \le C_4 \|v\|_{L^3}. \tag{22}$$

**Proof.** Since $\{\varphi_1, \ldots, \varphi_d\}$ is an orthonormal basis for $\mathcal{V}$ and $v \in \mathcal{V}$, there exist scalars $v_i = (v, \varphi_i)$, $i = 1, \ldots, d$, such that $v = \sum_{i=1}^{d} v_i \varphi_i$. Thus,

$$\|v\|_{L^3} = \left\| \sum_{i=1}^{d} v_i \varphi_i \right\|_{L^3} \le \sum_{i=1}^{d} |v_i| \, \|\varphi_i\|_{L^3} \le \left( \max_{i=1,\ldots,d} \|\varphi_i\|_{L^3} \right) \sum_{i=1}^{d} |v_i|. \tag{23}$$

By using Lemma 2.4-1 in [32], there is a constant $C > 0$ independent of $v$ such that

$$\sum_{i=1}^{d} |v_i| \le C \|v\|_{L^2}. \tag{24}$$

Inequalities (23) and (24) clearly imply the first inequality in (22). The other inequality is derived in a similar fashion. □

**Remark 4.1.** Although the constants $\max_{i=1,\ldots,d} \|\varphi_i\|_{L^3}$ in (23) and $C$ in (24) do not depend on $r$, they might depend on $m$. We notice that the dependence on $m$ also appears in the inverse estimate in Lemma 2 in [19] through the factor $\|S\|$ (with $S$ being the stiffness matrix $S_{ij} = (\phi_j', \phi_i')$). We emphasize, however, that this dependence on $m$ will disappear in the asymptotic limit $m \to \infty$ (or, equivalently, $\Delta t \to 0$). Since the error estimates we prove in this paper are for $\Delta t \to 0$, we can safely assume that $C_3$ and $C_4$ in (22) do not depend on $m$.

We next prove the following *a priori* stability estimates.

**Lemma 4.3.** *Assume that the solution to (12) satisfies $u' \in H_0^1$. Then the following stability estimates hold: there exist constants $C_5$, $C_6$ and $C_7$, such that, for all $k = 1, \ldots, m$, the following inequalities hold*

$$\|u'(t_k)\|_{L^2} \le C_5, \qquad \|u'(t_k)\|_{L^3} \le C_6, \quad \text{and} \quad \|P^r u'(t_k)\|_{L^3} \le C_7. \tag{25}$$

**Proof.** The first two inequalities in (25) follow immediately by letting $\varphi = u$ in (12), using $(F(u), u) = 0$, and (17) (the strong monotonicity of $G$). To prove the last inequality, we first use (6)

$$a(P^r u', \psi) = a(u', \psi) \quad \forall \psi \in S^r. \tag{26}$$

Next, we let $\psi := P^r u'$ in (26):

$$a(P^r u', P^r u') = a(u', P^r u'). \tag{27}$$

We then use the continuity of $a$ (15) in (27):

$$a(u', P^r u') \le \beta \|P^r u'\|_{L^2} \|u'\|_{L^2} \le \beta C_4 \|P^r u'\|_{L^3} \|u'\|_{L^2}. \tag{28}$$

On the other hand, using the coercivity of $a$ (16) in (27), we get

$$a(P^r u', P^r u') \ge \kappa \|P^r u'\|_{L^2}^2 \ge \kappa C_3^{-2} \|P^r u'\|_{L^3}^2. \tag{29}$$

Thus, (27)–(29) imply the last inequality in (25). □

We are now ready to prove the main result of this section.

**Theorem 4.1.** *Let $u$ be the solution of (12) and $\{U_k\}_{k=1}^m$ be the solution of (13). Assume that $u' \in H_0^1$ and $u_{tt} \in L^2(0,T;L^2)$. If $\Delta t$ is small enough, then there exists a constant $C > 0$, such that*

$$\frac{1}{m}\sum_{k=1}^{m}\|U_k - u(t_k)\|^2 \le C\left(\|u_0 - P^r u_0\|^2 + \sum_{k=r+1}^{d}\lambda_k + \Delta t^2\right). \tag{30}$$

**Proof.** The proof follows along the same lines as the proofs of Theorems 7 and 11 in [19]. Therefore, we highlight the main differences and only sketch the rest of the proof. We start by decomposing the error as

$$U_k - u(t_k) = U_k - P^r u(t_k) + P^r u(t_k) - u(t_k) = \vartheta_k + \varrho_k, \tag{31}$$

where $\vartheta_k := U_k - P^r u(t_k)$ and $\varrho_k := P^r u(t_k) - u(t_k)$. Clearly, we have

$$\frac{1}{m}\sum_{k=1}^{m}\|U_k - u(t_k)\|^2 \le \frac{2}{m}\sum_{k=1}^{m}\|\vartheta_k\|^2 + \frac{2}{m}\sum_{k=1}^{m}\|\varrho_k\|^2. \tag{32}$$

The approximation properties (20)–(21) and Poincaré's inequality (14) imply

$$\frac{1}{m}\sum_{k=1}^{m}\|\varrho_k\|^2 \le C_8\sum_{k=r+1}^{d}\lambda_k. \tag{33}$$

We now introduce the following notation: For $k = 1,\dots,m$, $\overline{\partial}\vartheta_k := \frac{\vartheta_k - \vartheta_{k-1}}{\Delta t}$, $v_k := u_t(t_k) - \overline{\partial}P^r u(t_k) = w_k + z_k$, $w_k := u_t(t_k) - \overline{\partial}u(t_k)$, $z_k := \overline{\partial}u(t_k) - \overline{\partial}P^r u(t_k)$. For all $\psi \in S^r$, we have

$$\begin{aligned}(\overline{\partial}\vartheta_k,\psi) + a(\vartheta_k,\psi) &= (\overline{\partial}U_k,\psi) + a(U_k,\psi) - (\overline{\partial}P^r u(t_k),\psi) - a(P^r u(t_k),\psi)\\ &= (f(t_k),\psi) - (F(U_k),\psi) - (G(U_k),\psi) - (\overline{\partial}P^r u(t_k),\psi) - a(u(t_k),\psi)\\ &= (v_k,\psi) + (F(u(t_k)) - F(U_k),\psi) + (G(u(t_k)) - G(U_k),\psi).\end{aligned}$$

By letting $\psi := \vartheta_k$ in the above equation, we get

$$\|\vartheta_k\|^2 - (\vartheta_k,\vartheta_{k-1}) + \Delta t\,\nu\,\|\vartheta_k'\|^2 = \Delta t\,(v_k,\vartheta_k) + \Delta t\,(F(u(t_k)) - F(U_k),\vartheta_k) + \Delta t\,(G(u(t_k)) - G(U_k),\vartheta_k). \tag{34}$$

We now have to estimate the terms on the RHS of (34). To this end, we follow [19] (see page 139). First, by using the Cauchy–Schwartz inequality, we get

$$(v_k,\vartheta_k) \le \|v_k\|\,\|\vartheta_k\|. \tag{35}$$

Then, exactly as in [19], we get

$$|(F(u(t_k)) - F(U_k),\vartheta_k)| \le \nu\,\|\vartheta_k\|_1^2 + C_9\,\|\vartheta_k\|^2 + C_{10}\,\|\varrho_k\|_1^2. \tag{36}$$

The last term on the RHS of (34), however, needs to be treated differently, since it did not show up in the analysis in [19]. We start by adding and subtracting terms

$$(G(u(t_k)) - G(U_k),\vartheta_k) = (G(u(t_k)) - G(P^r u(t_k)),\vartheta_k) + (G(P^r u(t_k)) - G(U_k),\vartheta_k). \tag{37}$$

We now move the last term on the RHS of (37) to the LHS of (34) (and thus change its sign) and apply the strong monotonicity property of $G$ (17) to obtain

$$(G(U_k) - G(P^r u(t_k)),\vartheta_k) \ge C_{11}\,\|\vartheta_k'\|_{L^3}^3. \tag{38}$$

For the first term on the RHS of (37), we need to apply the Lipschitz continuity of $G$ (18):

$$(G(u(t_k)) - G(P^r u(t_k)),\vartheta_k) \le CM\|\rho_k'\|_{L^3}\,\|\vartheta_k'\|_{L^3}, \tag{39}$$

where $M = \max\{\|u'(t_k)\|_{L^3}, \|P^r u'(t_k)\|_{L^3}\}$. Here we have used the stability of $u'(t_k)$ and $P^r u'(t_k)$ in the $L^3$ norm, which we proved in Lemma 4.3.

To estimate the term on the RHS of (39), we use the inverse estimates in Lemma 4.2 and the Cauchy–Schwartz inequality:

$$\|\rho_k'\|_{L^3}\,\|\vartheta_k'\|_{L^3} \le C_3^2\,\|\rho_k'\|\,\|\vartheta_k'\| \le \frac{\nu\,\|\vartheta_k'\|^2}{2} + \frac{1}{2\,\nu}C_3^4\,\|\rho_k'\|^2. \tag{40}$$

The rest of the proof now follows exactly as in [19]. Specifically, by using (35)–(40) in (34), by choosing $\Delta t$ sufficiently small, and by summing over $k$, we get

$$\|\vartheta_k'\|^2 \leq e^{C_{12}T}\left(\|\vartheta_0'\|^2 + \Delta t \sum_{j=1}^{k}\left(\|v_j\|^2 + C_{13}\|\rho\|_1^2\right)\right). \tag{41}$$

By using (33) and the estimates for $v_k$ in the proof of Theorem 7 in [19], we get (30). □

## 5. Numerical results

The goal of this section is twofold: First, it will provide numerical evidence for the improved performance of the POD–AV model (13) over the simple POD Galerkin truncation (11). Second, the numerical results will illustrate the theoretical estimate proved in Theorem 4.1. Our numerical study is presented in the context of the Burgers equation. We emphasize again that Burgers equation (5), while being commonly used as a one-dimensional approximation of the Navier–Stokes equations, does not model turbulence. We use it, however, for simplicity and clarity of exposition.

The following numerical discretization has been used in all our numerical tests. We used a finite element discretization in space. The computational domain $\Omega = [0, 1]$ was uniformly discretized and the finite element space used was piecewise linears. We used backward Euler for the temporal discretization. The nonlinearity in (5) was treated with a Newton iteration that was stopped when the norm of the difference between two consecutive iterations was less than $10^{-8}$. All computations were carried out using MATLAB.

We consider two test problems. Both problems develop shock-like phenomena that are challenging to capture with the usual POD Galerkin truncation (11). For both test problems we provide graphical illustrations of the improvement in accuracy for the POD–AV model (13) over the usual POD Galerkin truncation (11). To illustrate the theoretical estimate in Theorem 4.1, we also present tables with error convergence rates with respect to the number of POD modes.

### 5.1. Experiment 1

This test problem is similar to that used in [19]. The initial condition in (5) is

$$u_0(x) = \begin{cases} 1 & \text{if } x \in \left(0, \frac{1}{2}\right] \\ 0 & \text{if } x \in \left(\frac{1}{2}, 1\right). \end{cases} \tag{42}$$

The boundary conditions in (5) are homogeneous Dirichlet $u(0, t) = u(1, t) = 0$ for all $t$, the forcing term is $f = 0$, and the time interval is $[0, T] = [0, 1]$. The following parameters were used in the numerical discretization: Number of equally spaced mesh-points $n = 2048$ (which implies a mesh-size $\Delta x = 1/2048$); time-step $\Delta t = 10^{-3}$; diffusion parameter $\nu = 10^{-5}$; number of snapshots $m + 1 = 1001$. We deliberately chose a small value for $\nu$, since this would be similar to choosing a large Reynolds number in the Navier–Stokes equations. We also chose relatively small values for $\Delta t$ and $\Delta x$, since the main goal of this study is to investigate the contribution to the total error of the POD truncation and modeling, and not the contribution of spatial and temporal discretization.

We first ran a direct numerical simulation (DNS). Indeed, given the spatial and temporal resolutions used, we can safely consider the results of the Galerkin finite element discretization in Fig. 1 as our benchmark solution. The 1001 snapshots were used to generate the POD modes. We followed [19] and we did not include $\bar{\partial} u(t_k)$, since we used a small time-step $\Delta t$. The first 20 POD modes were used to run (i) the POD Galerkin truncation (11); and (ii) the POD–AV model (13) with $c = 10^{-4}$.

The time evolutions of the two models are presented in Figs. 2 and 3. Notice the clear improvement in solution accuracy in the POD–AV model. Indeed, the large numerical oscillations of the POD Galerkin truncation are dramatically decreased by the POD–AV model. A better visualization of this improvement is given in Fig. 4, where results from both POD models are compared with the "truth" (DNS) solution at the final time $T = 1$.

A quantitative illustration of the theoretical estimate (30) in Theorem 4.1 is given in Table 1. We present the $L^2$ norms of the errors for both models—the POD Galerkin truncation (11) (third column) and the POD–AV model (13) (fourth column). As noticed earlier, the spatial and temporal discretizations account only for a small percentage of the total error. Indeed, since $\Delta t = 10^{-3}$ and $\Delta x = 1/2048$, the first and third terms on the right-hand side of the inequality (30) in Theorem 4.1 are much smaller than the second term, which represents the POD truncation and modeling errors. The number of POD modes (first column) was chosen so that the POD truncation errors (second column) decrease by a factor of 2. As indicated by the theoretical estimate in [19], the square of the errors of the POD Galerkin truncation should decrease by a factor of 4. This behavior is observed in the third column of Table 1 (for $r \geq 20$). The numerical results for the POD–AV model (in the fourth column) are, as expected, much better than those of the POD Galerkin truncation (third column). They, however, do not seem to follow the theoretical estimate (30) in Theorem 4.1. We think that this is due to the fact that the POD truncation and modeling error in the POD–AV model initially dominates the spatial and temporal discretization errors, but once it reaches a certain threshold, the latter become significant.

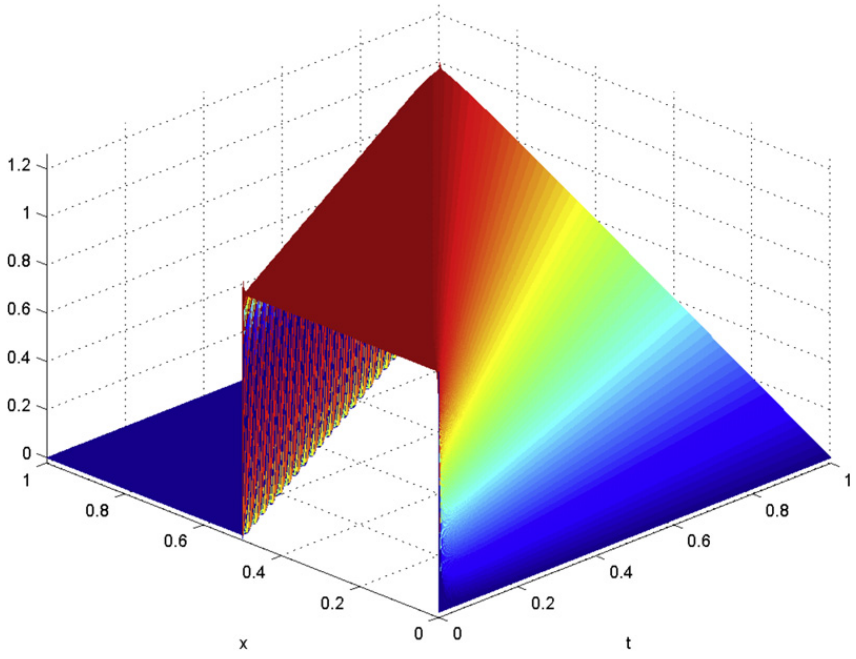


**Fig. 1.** Experiment 1: direct numerical simulation.

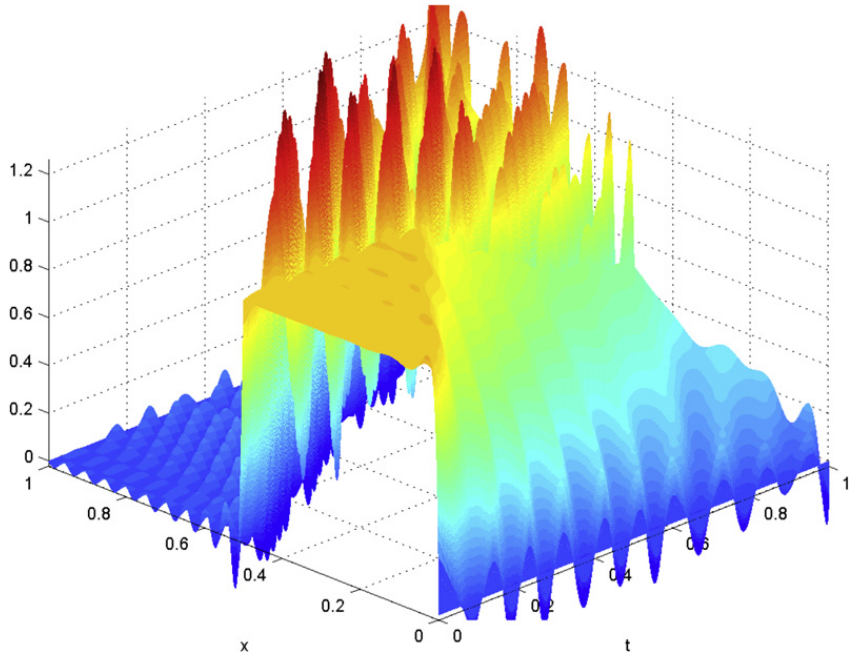


**Fig. 2.** Experiment 1: POD Galerkin truncation (11). Notice the poor quality of the approximations.

### 5.2. Experiment 2

This test problem is similar to that used in [33]. We simulate the propagation of an initial Gaussian disturbance given by

$$u_0(x) = \frac{10}{5\sqrt{\pi}} \exp\left(-\frac{(x-50)^2}{\omega}\right), \tag{43}$$

where $\omega = 400$ is the initial width of the wave and $t \in [0, 600]$. We rescale parameters so that $x \in [0, 1]$. Thus, the time interval becomes $[0, 1.5]$ and $\nu = 0.015/400 = 3.75 \times 10^{-5}$.

The boundary conditions in (5) are homogeneous Dirichlet $u(0, t) = u(1, t) = 0$ for all $t$ and the forcing term is $f = 0$. The following parameters were used in the numerical discretization: Number of equally spaced mesh-points $n = 2048$ (which implies a mesh-size $\Delta x = 1/2048$); time-step $\Delta t = 10^{-3}$; number of snapshots $m + 1 = 1001$. As in the first numerical example, we again chose a small value for $\nu$ and relatively small values for $\Delta t$ and $\Delta x$ (Fig. 5).

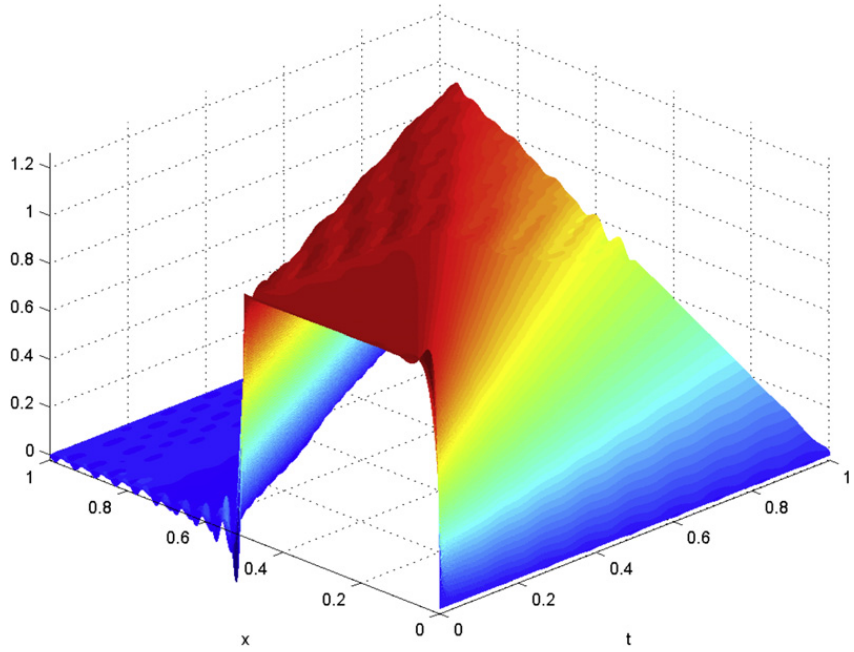


**Fig. 3.** Experiment 1: POD–AV model (13). Notice the significant improvement over the POD Galerkin truncation.

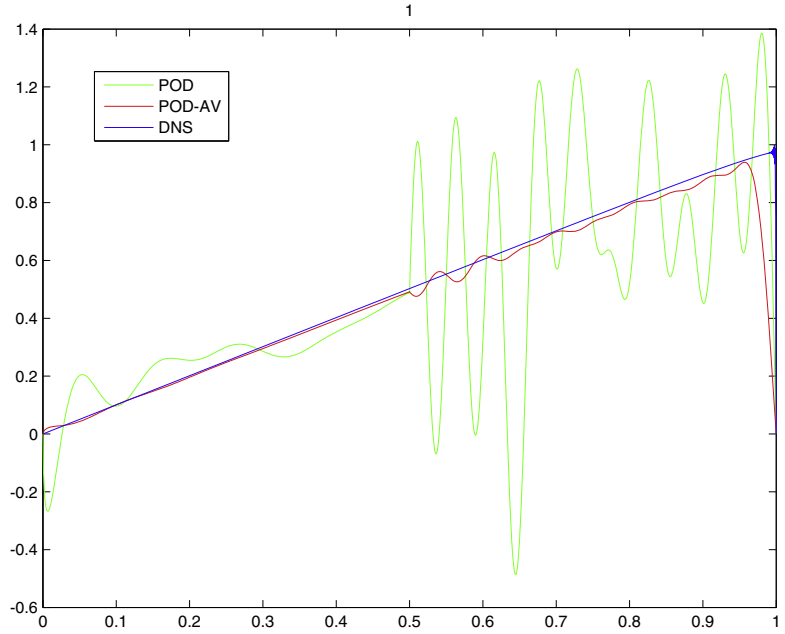


**Fig. 4.** Experiment 1: snapshots of DNS, POD Galerkin truncation and POD–AV models at the final time $T = 1$. Notice the significant improvement of the POD–AV model over the POD Galerkin truncation.

**Table 1**
Experiment 1: average errors for POD Galerkin truncation (11) and POD–AV model (13).

| $r$ | Normalized energy $\frac{\sum_{i=r}^{1001}\lambda_i}{\sum_{i=1}^{1001}\lambda_i}$ | POD | POD–AV |
|---|---|---|---|
| 6 | 0.0223 | 0.0778 | 0.0305 |
| 11 | 0.0111 | 0.0943 | 0.0090 |
| 20 | 0.0056 | 0.0428 | 0.0053 |
| 36 | 0.0028 | 0.0130 | 0.0051 |
| 62 | 0.0014 | 0.0038 | 0.0050 |

We first ran a DNS that we consider as our benchmark solution. The 1001 snapshots were used to generate the POD modes. We followed [19] and we have not included $\overline{\partial u}(t_k)$ since we used a small time-step $\Delta t$. The first 20 POD modes are used to run (i) the POD Galerkin truncation (11); and (ii) the POD–AV model (13) with $c = 5 \times 10^{-5}$.

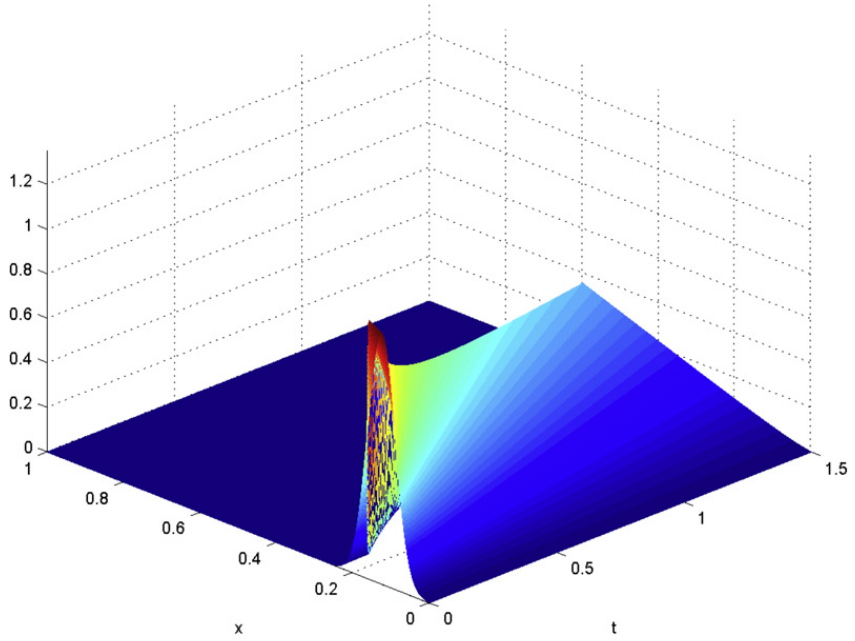


**Fig. 5.** Experiment 2: direct numerical simulation.

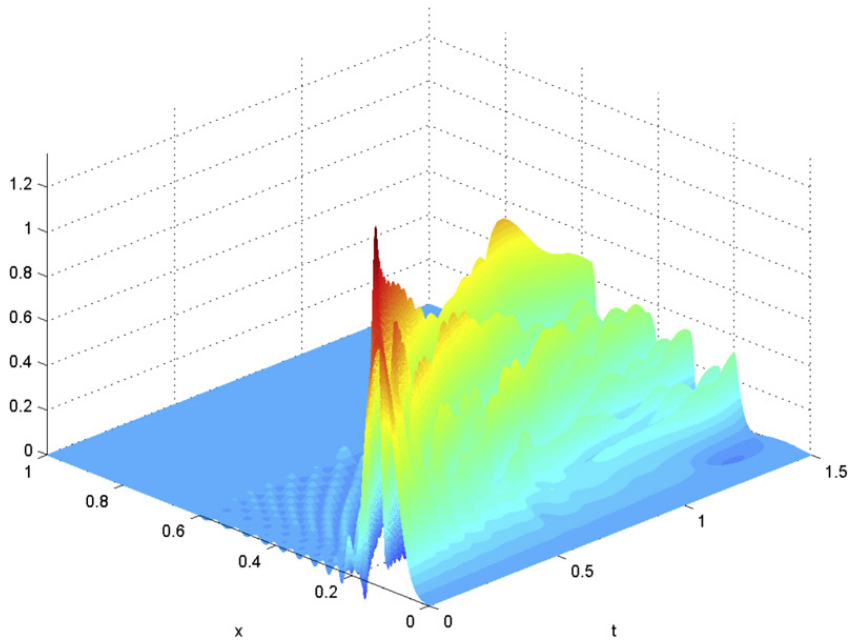


**Fig. 6.** Experiment 2: POD Galerkin truncation (11). Notice the poor quality of the approximations.

**Table 2**
Experiment 2: average errors for POD Galerkin truncation (11) and POD–AV model (13).

| $r$ | Normalized energy $\frac{\sum_{i=r}^{858}\lambda_i}{\sum_{i=1}^{858}\lambda_i}$ | POD | POD–AV |
|---|---|---|---|
| 6 | 0.0702 | 0.0358 | 0.0118 |
| 11 | 0.0345 | 0.0562 | 0.0022 |
| 20 | 0.0167 | 0.0263 | 8.78e−4 |
| 34 | 0.0085 | 0.0056 | 7.56e−4 |
| 56 | 0.0042 | 0.0009 | 7.44e−4 |

The time evolutions of the two models are presented in Figs. 6 and 7. As in the first numerical example, there is a clear improvement in solution accuracy in the POD–AV model. Indeed, the large numerical oscillations of the POD Galerkin truncation are dramatically decreased by the POD–AV model (see also Fig. 8).

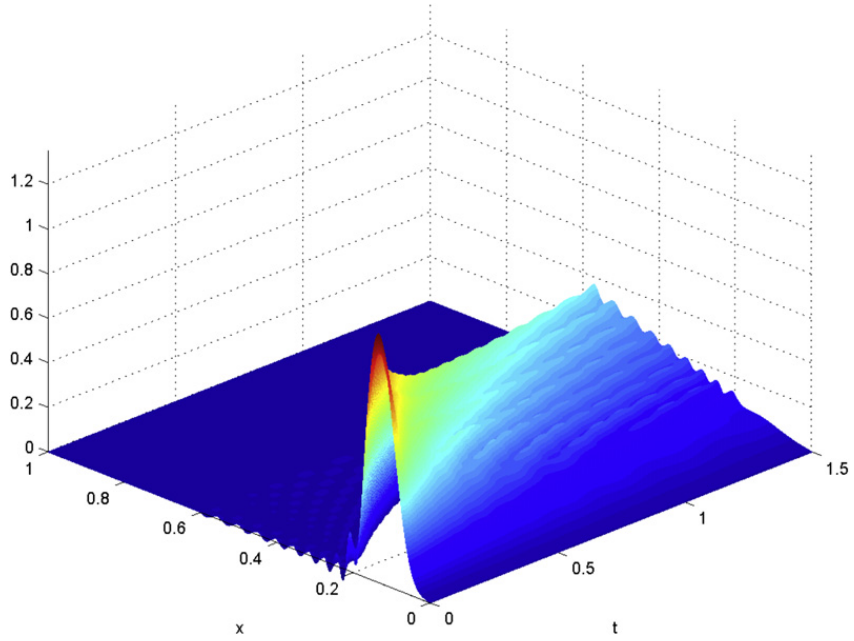


**Fig. 7.** Experiment 2: POD–AV model (13). Notice the significant improvement over the POD Galerkin truncation.

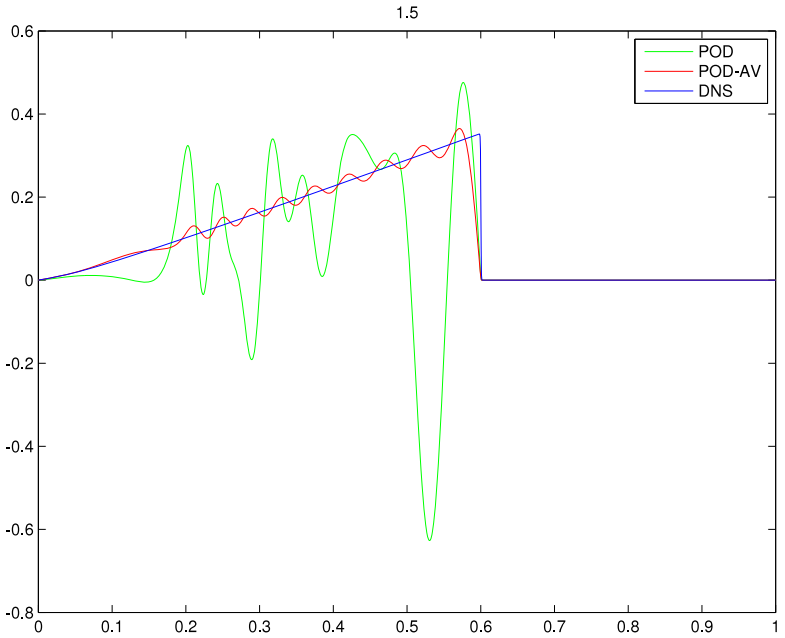


**Fig. 8.** Experiment 2: snapshots of DNS, POD Galerkin truncation and POD–AV models at the final time $T = 1.5$. Notice the significant improvement of the POD–AV model over the POD Galerkin truncation.

To illustrate the theoretical estimate (30) in Theorem 4.1, we present in Table 2 the $L^2$ norms of the errors for the POD Galerkin truncation (11) (third column) and the POD–AV model (13) (fourth column). As in the first numerical example, we notice that the numerical results for the POD–AV model are much better than those for the POD Galerkin truncation. We also notice that the error for the POD Galerkin truncation in the third column of Table 2 follow the theoretical estimates in [19] (for $r \geq 20$). Although the numerical results for the POD–AV model are much better than those of the POD Galerkin truncation, they do not seem to follow the theoretical estimate (30) in Theorem 4.1. We think that this behavior is due to the fact that for $r \geq 20$, the spatial and temporal discretization errors have the same order of magnitude as the POD truncation and modeling error.

## 6. Conclusions

In this paper, we have developed, analyzed and tested numerically a new reduced-order model that introduces an artificial viscosity term to account for the loss of information in the POD Galerkin truncation. Although similar models were

proposed in one of our earlier papers [34], this is the first time to our knowledge that such a model is analyzed and tested numerically. All theoretical and numerical results in this paper have been developed for Burgers equation (5). This choice allowed us a clear presentation of our results. We emphasize, however, that the new POD–AV model is by no means restricted to this one-dimensional setting. It is, in fact, developed for realistic turbulent flows.

Following [19], we presented a thorough numerical analysis for the discretization of the new POD–AV model. We proved the specific dependence of the total error on the temporal discretization and, more importantly, the dependence on the POD truncation. To test the new POD–AV model numerically, we used two test problems, both displaying shock-like behavior. In both tests, the POD–AV model clearly outperformed the usual Galerkin truncation by damping the numerical oscillations produced by the latter. The improved performance of the POD–AV model was displayed graphically as well as numerically.

These first steps in the assessment of the new POD–AV model are encouraging. There are, however, several steps that we need to take next. First and foremost, the new POD–AV model must be tested in a realistic turbulent flow, such as a turbulent pipe flow or flow past a cylinder. Second, the optimization of the constant $c$ in the POD–AV model might yield a significant improvement in the performance of the model. To this end, we will investigate the dependence of $c$ on different parameters, such as the number of POD modes and $\nu$. Finally, we believe that our new methodology could have a major impact in the reduced-order modeling and data assimilation of oceanic and atmospheric flows [35].

## Acknowledgements

The first author was partially supported by the National Science Foundation (DMS-0513542) and the Air Force Office for Scientific Research (FA9550-08-1-0136). The second author was partially supported by the National Science Foundation (DMS-0513542 and OCE-0620464) and the Air Force Office for Scientific Research (FA9550-08-1-0136). The third author was supported by the Air Force Office for Scientific Research (FA9550-08-1-0136).

## References

[1] C. Foiaş, O. Manley, R. Rosa, R. Temam, Navier Stokes Equations and Turbulence, Cambridge University Press, 2001.
[2] R. Temam, Infinite-Dimensional Dynamical Systems in Mechanics and Physics, second ed., in: Applied Mathematical Sciences, vol. 68, Springer-Verlag, New York, 1997.
[3] P. Holmes, J.L. Lumley, G. Berkooz, Turbulence, Coherent Structures, Dynamical Systems and Symmetry, Cambridge, 1996.
[4] L. Sirovich, Turbulence and the dynamics of coherent structures. I. Coherent structures, Quart. Appl. Math. 45 (3) (1987) 561–571.
[5] L. Sirovich, Turbulence and the dynamics of coherent structures. II. Symmetries and transformations, Quart. Appl. Math. 45 (3) (1987) 573–582.
[6] L. Sirovich, Turbulence and the dynamics of coherent structures. III. Dynamics and scaling, Quart. Appl. Math. 45 (3) (1987) 583–590.
[7] N. Aubry, P. Holmes, J.L. Lumley, E. Stone, The dynamics of coherent structures in the wall region of a turbulent boundary layer, J. Fluid Mech. 192 (1988) 115–173.
[8] K. Ito, S.S. Ravindran, A reduced-order method for simulation and control of fluid flows, J. Comput. Phys. 143 (2) (1998) 403–425.
[9] K. Kunisch, S. Volkwein, Control of the Burgers equation by a reduced-order approach using proper orthogonal decomposition, J. Optim. Theory Appl. 102 (2) (1999) 345–371.
[10] J.A. Atwell, B.B. King, Proper orthogonal decomposition for reduced basis feedback controllers for parabolic equations, Math. Comput. Modelling 33 (1–3) (2001) 1–19.
[11] H.V. Ly, H.T. Tran, Modeling and control of physical processes using proper orthogonal decomposition, Math. Comput. Modelling 33 (2001) 223–236.
[12] H.V. Ly, H.T. Tran, Proper orthogonal decomposition for flow calculations and optimal control in a horizontal CVD reactor, Quart. Appl. Math. 60 (4) (2002) 631–656.
[13] B.R. Noack, K. Afanasiev, M. Morzynski, G. Tadmor, F. Thiele, A hierarchy of low-dimensional models for the transient and post-transient cylinder wake, J. Fluid Mech. 497 (2003) 335–363.
[14] M. Buffoni, S. Camarri, A. Iollo, M.V. Salvetti, Low-dimensional modelling of a confined three-dimensional wake flow, J. Fluid Mech. 569 (1) (2006) 141–150.
[15] J.R. Singler, Transition to turbulence, small disturbances, and sensitivity analysis. I. A motivating problem, J. Math. Anal. Appl. 337 (2) (2008) 1425–1441.
[16] B. Podvin, On the adequacy of the ten-dimensional model for the wall layer, Phys. Fluids 13 (1) (2001) 210–224.
[17] B. Podvin, J. Lumley, A low-dimensional approach for the minimal flow unit, J. Fluid Mech. 362 (1998) 121–155.
[18] M. Couplet, P. Sagaut, C. Basdevant, Intermodal energy transfers in a proper orthogonal decomposition-Galerkin representation of a turbulent separated flow, J. Fluid Mech. 491 (2003) 275–284.
[19] K. Kunisch, S. Volkwein, Galerkin proper orthogonal decomposition methods for parabolic problems, Numer. Math. 90 (1) (2001) 117–148.
[20] R.A. Adams, Sobolev Spaces, in: Pure and Applied Mathematics, vol. 65, Academic Press, New York, London, 1975.
[21] J.S. Smagorinsky, General circulation experiments with the primitive equations, Mon. Weather Rev. 91 (1963) 99–164.
[22] L.C. Berselli, T. Iliescu, W.J. Layton, Mathematics of Large Eddy Simulation of Turbulent Flows, in: Scientific Computation, Springer-Verlag, Berlin, 2006.
[23] P. Sagaut, Large Eddy Simulation for Incompressible Flows, third ed., in: Scientific Computation, Springer-Verlag, Berlin, 2006.
[24] K. Kunisch, S. Volkwein, Galerkin proper orthogonal decomposition methods for a general equation in fluid dynamics, SIAM J. Numer. Anal. 40 (2) (2002) 492–515. (electronic).
[25] Z. Luo, J. Chen, I.M. Navon, X. Yang, Mixed finite element formulation and error estimates based on proper orthogonal decomposition for the nonstationary Navier–Stokes equations, SIAM J. Numer. Anal. 47 (1) (2008) 1–19.
[26] C. Homescu, L.R. Petzold, R. Serban, Error estimation for reduced-order models of dynamical systems, SIAM J. Numer. Anal. 43 (4) (2005) 1693–1714. (electronic).
[27] J.-L. Lions, Quelque méthodes de résolution des problemès aux limitex non linéaires, Dunod, Gauthier–Villars, Paris, 1969.
[28] G.J. Minty, Monotone (nonlinear) operators in Hilbert space, Duke Math. J. 29 (1962) 341–346.
[29] Q. Du, M.D. Gunzburger, Finite-element approximations of a Ladyzhenskaya model for stationary incompressible viscous flow, SIAM J. Numer. Anal. 27 (1990) 1–19.
[30] Q. Du, M.D. Gunzburger, Analysis of a Ladyzhenskaya model for incompressible viscous flow, J. Math. Anal. Appl. 155 (1991) 21–45.
[31] H.V. Ly, K.D. Mease, E.S. Titi, Distributed and boundary control of the viscous Burgers' equation, Numer. Funct. Anal. Optim. 18 (1–2) (1997) 143–188.
[32] E. Kreyszig, Introductory Functional Analysis with Applications, in: Wiley Classics Library, John Wiley & Sons Inc., New York, 1989.
[33] K. Mohseni, H. Zhao, J.E. Marsden, Shock regularization for Burgers equation, in: 44th AIAA Aerospace Sciences Meeting and Exhibit, Reno, NV, AIAA Paper 2006-1516, January 2006.
[34] J.T. Borggaard, A. Duggleby, A. Hay, T. Iliescu, Z. Wang, Reduced-order modeling of turbulent flows, in: Proceedings of MTNS, 2008.
[35] F. Fang, C.C. Pain, I.M. Navon, G.J. Gorman, M.D. Piggott, P.A. Allison, A.J.H. Goddard, A POD reduced order unstructured mesh ocean modelling method for moderate Reynolds number flows, Internat. J. Numer. Methods Fluids (2008).